Oblique-plane single-molecule localization microscopy for tissues and small intact animals

Jeongmin Kim [1,2], Michal Wojcik [3], Yuan Wang[1,2], Seonah Moon[3], Emilia A. Zin[4], Nadia Marnani[5], Zachary L. Newman[5], John G. Flannery [4,5], Ke Xu [3,6,7]* and Xiang Zhang [1,2]*

Single-molecule localization microscopy (SMLM), while well established for cultured cells, is not yet fully compatible with tissue-scale samples. We introduce single-molecule oblique-plane microscopy (obSTORM), which by directly imaging oblique sections of samples with oblique light-sheet illumination offers a deep and volumetric SMLM platform that is convenient for standard tissue samples and small intact animals. We demonstrate super-resolution imaging at depths of up to 66 μm for cells, *Caenorhabditis elegans* gonads, *Drosophila melanogaster* larval brain, mouse retina and brain sections, and whole stickleback fish.

SMLM[1–3] has become an important optical imaging tool for biology owing to its nanoscale resolution. As superior precision of localization results from quality single-molecule detection at high signal-to-background ratios (SBRs)[4], conventional SMLM systems often employ sub-critical-angle epi-illumination[5] using high-numerical-aperture (NA), oil-immersion objectives to confine light within depths of a few micrometers in aqueous samples. This intended refractive index mismatch restricts the accessible imaging depth to only a few micrometers[6], and thus applications are mostly bound to either thin samples like cultured cells or regions of samples near coverslips. Recently, there have been substantial improvements in the detection depth of deep-tissue SMLM[7,8], yet the illumination used is still not optimal for deep imaging and provides limited capabilities for optical sectioning and volumetric localization.

Alternatively, light-sheet illumination in a two-objective configuration[9] enables excellent optical sectioning and high-SBR imaging in refraction index-matched environments, thus facilitating deeper SMLM imaging[10]. Recent reflected-light-sheet SMLM methods[11–15] that use specialized geometry and/or devices for samples have improved spatial resolution within depths of 6–30 μm. While these SMLM methods are well suited for whole cells[11–13], cell aggregates[14] and even thicker samples (for example, peripheral regions of embryos[15]), the laterally propagating light sheet is not directly applicable to laterally extended samples like ordinary tissue slices (>1 mm in width). In principle, smaller regions of interest can be isolated for SMLM imaging if they can be identified, but such approaches may be inconvenient and lead to sample damage.

Here we report obSTORM, a light-sheet SMLM approach that works with any sample type mounted on regular coverslips, including tissues and small whole animals, thus expanding SMLM applications beyond the whole-cell scale. obSTORM captures an optical section along the oblique plane (*xo*) into the sample depth, which is enabled by angled light-sheet illumination and oblique-plane microscopy (OPM)[16–18] that optically conjugates the *xo* plane to the camera plane (Fig. 1a and Supplementary Fig. 1). To enable single-molecule OPM to image deep into samples, we designed a water-immersion-based system (O1; 1.2 NA) that is able to operate at higher angles (α of between 45° and 90°) while reducing the undesired ellipticity of the OPM point-spread function (PSF) through the use of a polarizing beam splitter, a quarter-wave plate and a remote objective (O2; 0.95 NA) of a larger cone angle than O1 (Supplementary Fig. 2 and Supplementary Note).

We first characterized the detection PSF of obSTORM. Our theoretical calculations and experimental measurements indicated near-circular PSFs for α values of between 0° and 50°, with an increase in full width at half-maximum (FWHM) of ~20% to ~400 nm as compared to that of conventional in-plane microscopy (~330 nm at 1.2 NA), and this value was further increased in the oblique direction (*o*) for higher angles (Fig. 1b,c and Supplementary Fig. 3 for emission at 685 and 570 nm, respectively). Nonetheless, the brightness and size of PSFs were reasonably maintained over an axial depth of 100 μm (Supplementary Fig. 4).

For Alexa Fluor 647 (AF647)-labeled microtubules (α-tubulin) in cultured A549 cells, obSTORM directly resolved the microtubule network throughout the cell depth along the 45° diagonal direction (Fig. 1d). The light efficiency in 45° obSTORM is ~25% that of conventional STORM owing to the following losses: 50% at the polarizing beam splitter, 26% at the remote objective (double pass) and 30% at the asymmetric pupil (Fig. 1b). Thus, the average photon count of AF647 molecules was 954 (Supplementary Fig. 5). This value is still comparable to what is typically found in SMLM experiments based on dimmer dyes (for example, Atto488 and Nile Red) and fluorescent proteins (for example, mEos2), and single-molecule images were obtained with high contrast (Supplementary Fig. 5 and Supplementary Video 1). The average localization precision was ~18.5 nm for both the *x* and *o* directions through the entire cell depth (Supplementary Fig. 5), corresponding to an FWHM resolution of ~44 nm in both directions. In comparison, conventional three-dimensional (3D) STORM[6] achieves a lateral resolution of 25–30 nm and an axial resolution of 60–70 nm for thin samples. Two adjacent microtubules at a center-to-center distance of 128 nm were clearly resolved with an apparent width of ~69 nm for each microtubule (Fig. 1e). This width is consistent with a convolution of our resolution with the size of antibody-labeled microtubules (56 nm)[19], and was approximately fourfold smaller than that

[1]NSF Nanoscale Science and Engineering Center, University of California, Berkeley, Berkeley, CA, USA. [2]Materials Sciences Division, Lawrence Berkeley National Laboratory, Berkeley, CA, USA. [3]Department of Chemistry, University of California, Berkeley, Berkeley, CA, USA. [4]Vision Science, School of Optometry, University of California, Berkeley, Berkeley, CA, USA. [5]Department of Molecular and Cell Biology, University of California, Berkeley, Berkeley, CA, USA. [6]Division of Molecular Biophysics and Integrated Bioimaging, Lawrence Berkeley National Laboratory, Berkeley, CA, USA. [7]Chan Zuckerberg Biohub, San Francisco, CA, USA. *e-mail: xuk@berkeley.edu; xiang@berkeley.edu

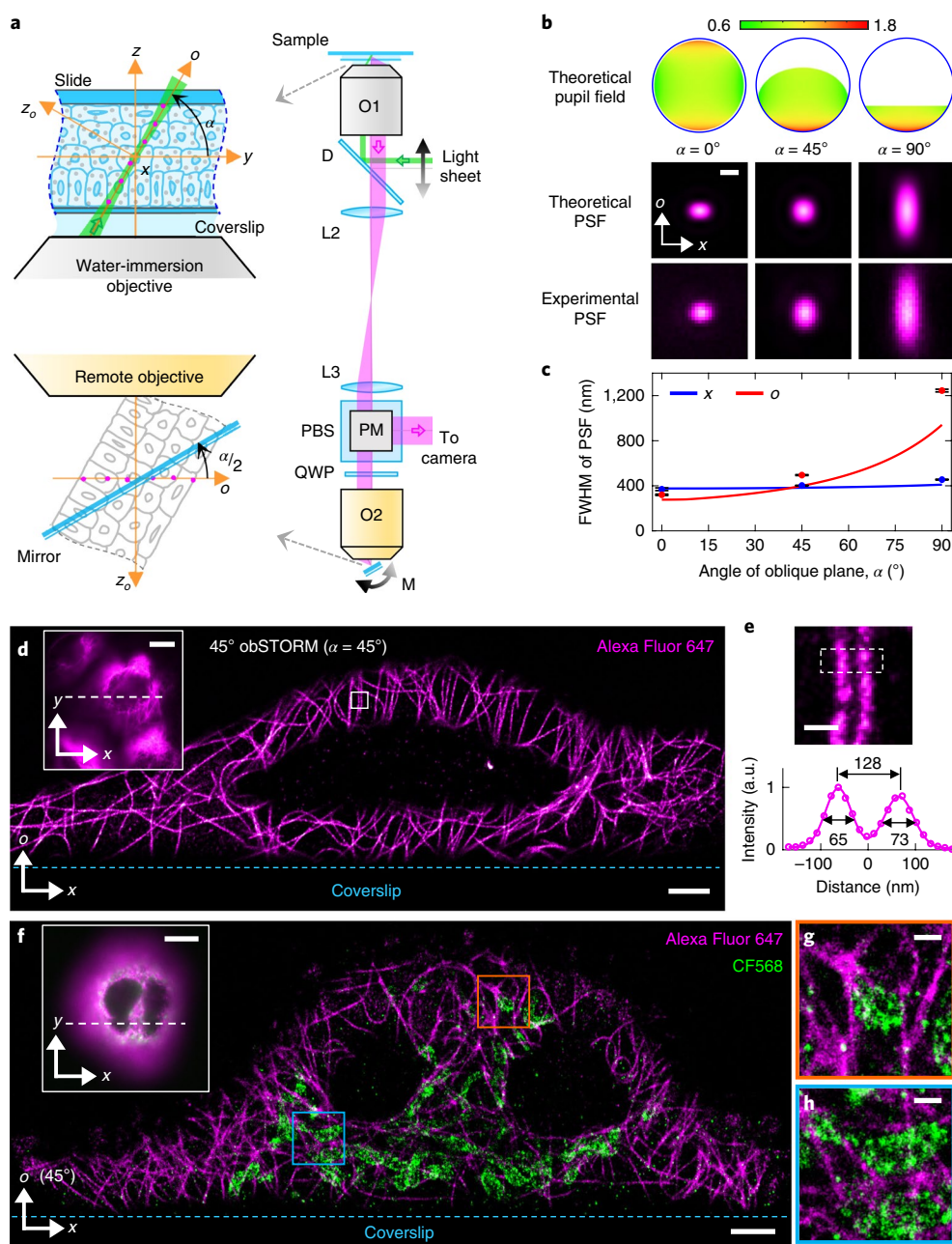**Fig. 1 | Imaging principle and cell-scale demonstration of obSTORM. a**, Schematic layout of obSTORM. A light sheet (green beam) excites and activates single molecules in a sample along the *xo* plane, which is inclined by (tunable) *α* from the focal plane of the O1 objective (1.2 NA). The emitted single molecules (magenta dots) are refocused onto the focal plane of the remote O2 objective (0.95 NA) by the *α*/2-angled mirror (M) and directly detected by a camera (magenta beam). D, dichroic beam splitter; L, lens; PBS, polarizing beam splitter; QWP, quarter-wave plate; PM, periscope mirror. **b**, Theoretical exit pupil fields (scaled to one at the pupil center) and PSFs at a wavelength of 685 nm, and representative PSF images measured with dark-red beads (from *n* = 9, 4 and 6 distinct beads at *α* = 0°, 45° and 90°, respectively). **c**, Comparison between theoretical FWHM (lines) of PSFs and experimental results. Data are plotted as mean ± s.d.; sample sizes are listed in **b**. **d**, obSTORM image of microtubules in an A549 cell at *α* = 45°. The inset image shows the diffraction-limited lateral-plane view with a white dashed line that intersects the oblique plane. **e**, Expanded view of the white boxed area in **d** (top) and the intensity profile across the two microtubules (bottom; after vertical binning within the white dashed area). **f**, Two-color 45° obSTORM image of microtubules (magenta) and mitochondria (green). The inset image shows the conventional lateral-plane image with the intersection line (white dashed). **g,h**, Expanded views of the two boxed regions in **f**. Images shown in **d,e** are representative of four cells and images shown in **f–h** are representative of another four cells. Scale bars, 400 nm (**b,g,h**), 2 μm (**d,f**), 10 μm (insets in **d** and **f**) and 200 nm (**e**).

obtained by conventional confocal microscopy with deconvolution (Supplementary Fig. 6). Comparable results were consistently found over A549 cells, and a network of hollow-shaped mitochondrial outer membranes (Tom20) was also successfully visualized (Supplementary Figs. 7 and 8).

Our approach is compatible with multicolor imaging after proper calibrations (Supplementary Figs. 9 and 10). For example, in our 45° two-color obSTORM images, mitochondria and microtubules in A549 cells (interchangeably labeled by CF568 and AF647) were both well resolved, and the former were correctly surrounded
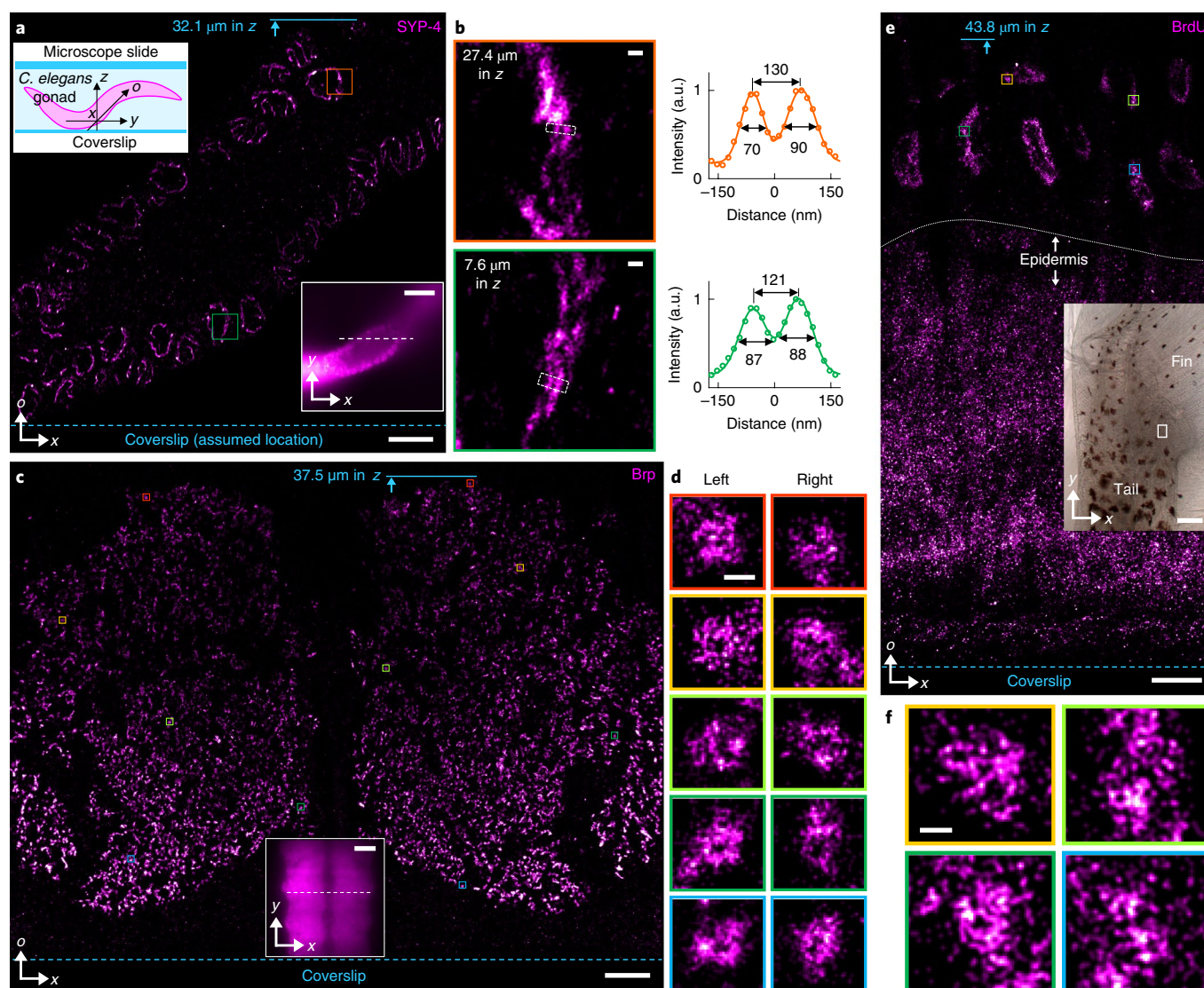
Fig. 2 | Tissue-scale super-resolution imaging enabled by 45° obSTORM. Tissues were labeled with AF647. **a**, Super-resolution image of SYP-4 in *C. elegans* germ cells. Inset images are an illustration of the worm gonad (top left) and the diffraction-limited lateral image (bottom right), with the dashed line intersecting the *xo* plane. **b**, Expanded views at two different depths from **a** (left) and cross-sectional intensity profiles (right). **c**, obSTORM image of Brp across the ventral nerve cord cross-section of a *Drosophila* larval brain along the dashed line in the diffraction-limited lateral view (inset). **d**, Expanded views over various field locations in **c** (five boxed regions on each side). The brightness of each image was rescaled. **e**, obSTORM image of DNA-incorporated BrdU in the caudal fin mesenchyme of an intact stickleback fish. The inset image shows the bright-field image of the fish tail and the area of obSTORM imaging (white box). **f**, Expanded views of four different nuclei from **e**. Images shown are representative of three images from two gonads (**a**,**b**), ten images from five larvae (**c**,**d**) and four images from two sticklebacks (**e**,**f**). Scale bars, 5 μm (**a**,**c**,**e**), 20 μm (insets in **a** and **c**), 100 μm (inset in **e**) and 200 nm (**b**,**d**,**f**).

by the latter (Fig. 1f–h and Supplementary Fig. 11). In addition to the 45° plane, we also imaged cells along the axial plane ($\alpha = 90°$) to show that, in principle, obSTORM enables any orientational view (Supplementary Figs. 12 and 13). Despite the reduced resolution, 90° obSTORM still resolved individual microtubules and the hollow structure of mitochondria and could be beneficial when the principal plane of interest of a sample (in two-dimensional imaging application) is axial[20], with potential resolution improvements discussed later.

For tissue- to whole-organism-scale demonstrations, we first imaged the synaptonemal complex protein SYP-4 of *C. elegans* gonads over 45.4 μm in the *o* direction, equivalent to 32.1 μm in the *z*-projected depth (Fig. 2a). Image features at ~87 nm in width and center-to-center distances of ~125 nm were resolved at different depths (Fig. 2b). Next, we imaged a *Drosophila* larval brain exposed

by minimal incisions of the larva, avoiding any extraction or sectioning of the brain (Supplementary Fig. 14). obSTORM reconstructed fine details of the dense Bruchpilot protein (Brp) structure across the whole ventral nerve cord cross-section, extending over 37 μm in the *z* direction (Fig. 2c). The donut shape of Brp[21] at ~200 nm in diameter was distinctly resolved throughout the brain depth (Fig. 2d), a result not achieved by confocal microscopy with deconvolution (Supplementary Fig. 14). For the mammalian tissue slice of mouse retina (100 μm thick), we imaged protein kinase C alpha (PKCα) at depths of up to 66 μm, which outlined the plasma membrane of rod bipolar cells (Supplementary Figs. 15 and 16). We further showed that the hollow shape of Tom20-labeled outer membranes of mitochondria in mouse retina and brain slices throughout depths of ~46 μm and ~40 μm, respectively, was resolved by obSTORM (Supplementary Figs. 17 and 18). Finally, we demonstrated
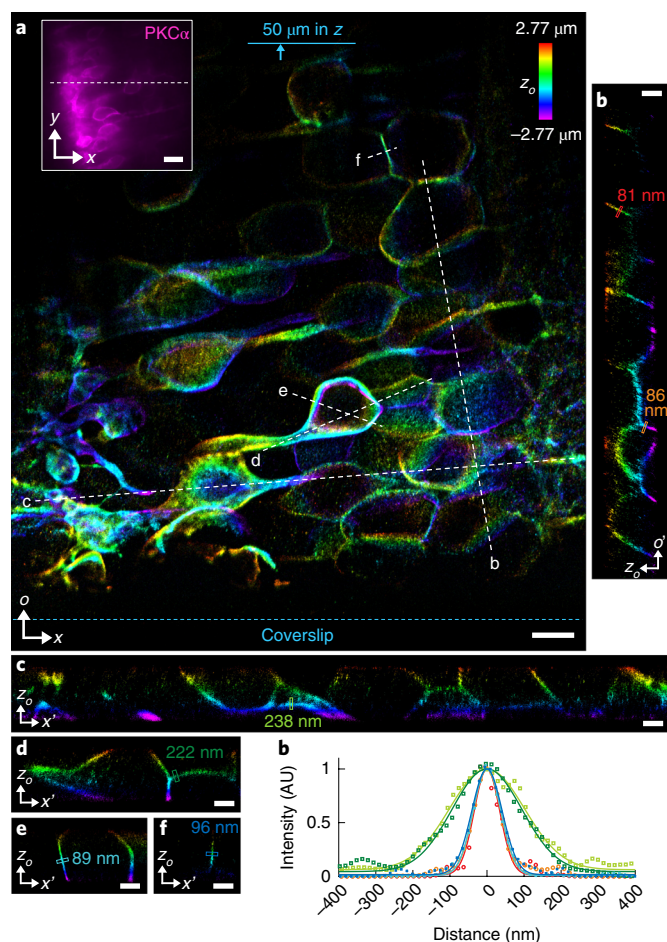
Fig. 3 | Volumetric super-resolution imaging of PKCα in 60-μm-thick mouse retina sections. a, Representative volumetric obSTORM image through a tissue depth of 50 μm ($n = 4$ volumetric image datasets from two retina slices), constructed from a stack of ten 45° obSTORM images (10,000 frames per optical section). Color encodes the third dimension (z_o) normal to the 45° oblique plane (xo). The inset image shows the diffraction-limited lateral-plane view, with the white dashed line marking where the obSTORM image was taken. **b–f**, Five cross-sectional views along the white dashed lines marked in **a**. The axes along the selected lines are labeled with either x' or o' according to the angular proximity to the x and o directions. **g**, Six intensity profiles across the membrane-like thin image features at different locations and orientations (boxed regions in **b–f**). The estimated FWHMs are shown near each box in **b–f**. Scale bars, 5 μm (**a**), 10 μm (inset in **a**) and 2 μm (**b–f**).

obSTORM for small whole animals by imaging 5-bromo-2′-deoxyuridine (BrdU) labeling in uncut juvenile stickleback fish of approximately 6 mm in length (Fig. 2e). The newly synthesized DNA in proliferating mesenchymal cells was thus visualized, without the need for cutting of the fish, up to depths of 44 μm through the ~30-μm-thick caudal fin epidermis (Fig. 2f).

We further achieved 3D obSTORM by adding a third dimension (z_o) of localization normal to the 45° oblique plane using astigmatic PSFs[22] with a section thickness of ~1 μm (Supplementary Fig. 19). Taking advantage of the optical sectioning capability of obSTORM, we next acquired a stack of ~10 oblique sections by z stepping the sample objective for volumetric reconstruction. Good volumetric super-resolution images were obtained for 60-μm-thick retina slices (Fig. 3 and Supplementary Figs. 20 and 21) over a volume of $70_{(x)} \times 71_{(o)} \times 5.4_{(z_o)}$ μm³. The membrane-like image feature signified

by PKCα was well visualized and measured to have an FWHM thickness of ~93, ~83 and ~230 nm in the x, o and z_o directions, respectively (Fig. 3b), attributable to the anisotropic localization precision (Supplementary Fig. 21).

Taking these findings together, we have shown good oblique and volumetric SMLM images as deep as 40–60 μm into diverse samples. Currently, the localization precision of 45° obSTORM with AF647 ranges from ~18 nm (thin cells) to ~26 nm (tissues) and ~40 nm (animals) (Supplementary Table 1), which is lower than conventional SMLM precision in thin samples, yet useful for tissue-scale applications when considering the deeper access, good optical sectioning and user-friendly sample preparation that it offers. Our localization analysis (Supplementary Figs. 22–29) revealed good uniformity through sample depth for cultured cells. For thick tissues, larger spatial variations were noted, primarily owing to non-uniform illumination and increased background fluorescence, the latter of which is probably due to a thicker light-sheet incident on samples (Supplementary Fig. 30) and its scattering-induced blur. A better refractive index match (for example, with glycerol immersion) may help reduce resolution degradation and further increase the depths of illumination and imaging. Moreover, resolution could be further improved by approximately 1.3× and 2.0× for α values at 45° and 90°, respectively, by using objectives with higher cone angles (Supplementary Fig. 31). The use of brighter fluorophores (for example, through dye caging[23]) may help further boost the achievable resolution. In addition, non-diffracting beams[24] may provide more uniform sheet illumination, thus possibly minimizing the spatial variation of localization precision.

As demonstrated, obSTORM offers super-resolution imaging along any oblique planes deep inside thick samples. The imaging platform has a geometry that is fully compatible with tissue- and higher-scale samples prepared by standard protocols, features volumetric super-resolution capability with selective plane illumination and allows multicolor imaging. obSTORM thus expands the applicability of SMLM technology broadly from cells to tissues and small intact animals.

Online content

Any methods, additional references, Nature Research reporting summaries, source data, statements of code and data availability and associated accession codes are available at https://doi.org/10.1038/s41592-019-0510-z.

References

1. Rust, M. J., Bates, M. & Zhuang, X. *Nat. Methods* **3**, 793–795 (2006).
2. Betzig, E. et al. *Science* **313**, 1642–1645 (2006).
3. Hess, S. T., Girirajan, T. P. K. & Mason, M. D. *Biophys. J.* **91**, 4258–4272 (2006).
4. Thompson, R. E., Larson, D. R. & Webb, W. W. *Biophys. J.* **82**, 2775–2783 (2002).
5. Tokunaga, M., Imamoto, N. & Sakata-Sogawa, K. *Nat. Methods* **5**, 159–161 (2008).
6. Huang, B., Jones, S. A., Brandenburg, B. & Zhuang, X. *Nat. Methods* **5**, 1047–1052 (2008).
7. Mlodzianoski, M. J. et al. *Nat. Methods* **15**, 583–586 (2018).
8. Bon, P. et al. *Nat. Methods* **15**, 449–454 (2018).
9. Huisken, J., Swoger, J., Del Bene, F., Wittbrodt, J. & Stelzer, E. H. K. *Science* **305**, 1007–1009 (2004).
10. Cella Zanacchi, F. et al. *Nat. Methods* **8**, 1047–1049 (2011).
11. Gebhardt, J. C. M. et al. *Nat. Methods* **10**, 421–426 (2013).
12. Meddens, M. B. M. et al. *Biomed. Opt. Express* **7**, 2219–2236 (2016).
13. Gustavsson, A.-K., Petrov, P. N., Lee, M. Y., Shechtman, Y. & Moerner, W. E. *Nat. Commun.* **9**, 123 (2018).
14. Galland, R. et al. *Nat. Methods* **12**, 641–644 (2015).
15. Greiss, F., Deligiannaki, M., Jung, C., Gaul, U. & Braun, D. *Biophys. J.* **110**, 939–946 (2016).
16. Dunsby, C. *Opt. Express* **16**, 20306–20316 (2008).
17. Kim, J., Li, T., Wang, Y. & Zhang, X. *Opt. Express* **22**, 11140–11151 (2014).
18. Li, T. et al. *Sci. Rep.* **4**, 7253 (2014).

19. Bates, M., Huang, B., Dempsey, G. T. & Zhuang, X. *Science* **317**, 1749–1753 (2007).
20. Chaudhuri, O., Parekh, S. H., Lam, W. A. & Fletcher, D. A. *Nat. Methods* **6**, 383–387 (2009).
21. Kittel, R. J. et al. *Science* **312**, 1051–1054 (2006).
22. Huang, B., Wang, W., Bates, M. & Zhuang, X. *Science* **319**, 810–813 (2008).
23. Vaughan, J. C., Jia, S. & Zhuang, X. *Nat. Methods* **9**, 1181–1184 (2012).
24. Vettenburg, T. et al. *Nat. Methods* **11**, 541–544 (2014).

Author contributions

J.K. designed and built the microscopy system, calculated theoretical PSFs, prepared fluorescent bead samples, calibrated the optical system and wrote software code for localization analysis. M.W. and S.M. prepared cell samples. S.M. labeled mouse brain tissues. E.A.Z. and J.G.F. prepared retina samples and provided fixed brain sections. N.M. and Z.L.N. prepared *Drosophila* samples. J.K. and M.W. carried out imaging experiments. J.K. and Y.W. analyzed single-molecule data. X.Z. and K.X. guided the research. J.K., M.W., Y.W., K.X. and X.Z. contributed to writing the manuscript.

Competing interests

J.K., Y.W. and X.Z. have filed a provisional patent application on the microscopy system and method.

Additional information

Supplementary information is available for this paper at https://doi.org/10.1038/s41592-019-0510-z.

Reprints and permissions information is available at www.nature.com/reprints.

Correspondence and requests for materials should be addressed to K.X. or X.Z.

Peer review information: Rita Strack was the primary editor on this article and managed its editorial process and peer review in collaboration with the rest of the editorial team.

Publisher's note: Springer Nature remains neutral with regard to jurisdictional claims in published maps and institutional affiliations.

Methods

The optical setup of obSTORM. The microscope was built on an optical table as illustrated in Supplementary Fig. 1. Three diode-pumped solid-state lasers were used for single-molecule excitation at wavelengths of 641 nm (40 mW; OBIS 640LX-40, Coherent) and 532 nm (1,300 mW; Newgazer Tech) and for activation at a wavelength of 405 nm (300 mW; Newgazer Tech). We coupled each laser beam to individual single-mode fibers (S405-XP, Thorlabs) to improve beam profile quality. After being collimated at e^{-2} diameters of 1.3–1.6 mm and combined by two dichroic mirrors (T588lpxr-UF2, Chroma; and Di03-R488, Semrock), the three laser beams were shaped into slit beams by horizontal focusing with a cylindrical lens (CL; $f_{CL} = 250$ mm (ACY254-250-A) or $f_{CL} = 500$ mm (LJ1144RM-A), Thorlabs) and vertical expansion with a pair of cylindrical lenses (ACY254-050-A and ACY254-200-A, Thorlabs). The formed slit beams were steered on a gimbal mirror, reflected at a dichroic beam splitter (Di03-R405/488/532/635, Semrock) and demagnified by a $4f$ system comprising the L1 lens (ACH254-200-A, Thorlabs) and a water-immersion objective (O1; UPLSAPO 60XW/1.20, Olympus) with a piezo scanner (P-721, Physik Instrumente). The e^{-2} waist thickness of light sheets measured at $\alpha = 90°$ with $f_{CL} = 250$ mm was ~1.6 and ~2.1 µm for the 532-nm and 641-nm light, respectively, or doubled with $f_{CL} = 500$ mm for thicker samples (Supplementary Fig. 30). For wide-field epi-illumination, the collimated laser beams were bypassed by two mirrors with flipper optic mounts (9891, Newport) and expanded by 5.4× using a pair of lenses (M-10X, Newport; and #49-782, Edmund Optics). The light-sheet illumination covers $\alpha = 45–90°$, and the wide-field illumination could cover $\alpha = 0–45°$ for thin samples at compromised SBRs.

For fluorescence detection, we conjugated the back focal planes of O1 and the remote objective (O2; MPlanApo 50×/0.95, Olympus) by a $4f$ system of two lenses (L2, $f = 200$ mm (#47–645, Edmund Optics); and L3 (AC508-180-A, Thorlabs)). We prepared the following three remote mirrors: a silver mirror (PF10-03-P01, Thorlabs) for $\alpha = 0°$; a gold-evaporated silicon wafer mirror (10 mm × 15 mm, homemade) attached on the 22.5° surface of a pentaprism (PS-932, Thorlabs) for $\alpha = 45°$; and a right-angle prism mirror (MRAK25-P01, Thorlabs) for $\alpha = 90°$. These mirrors were either housed by, or glued on, lens tubes (SM1L series, Thorlabs) for convenient switching on a kinematic rotation mount (KS1RS, Thorlabs), which was affixed on a two-dimensional stage (462-XY-SD, Newport) and driven by piezo actuators (NPM140SG, Newport). A single small mirror, in principle, can cover all angles ($\alpha = 0–90°$) with proper control of its rotation and translation. Notably, our single-objective layout at both sample and remote spaces allows higher α values and makes it easier to increase effective NA (using objectives with larger cone angles, for example, TIRF objectives) with no mechanical interference[16,25]. We used a polarizing beam splitter (CCM1-PBS251, Thorlabs) and an achromatic quarter-wave plate (AQWP05M-600, Thorlabs) to intensify the vertical edges of fluorescence signals at the exit pupil (Fig. 1b), which mitigates the ellipticity of PSFs at higher α values owing to the asymmetric pupil loss (for example, 30% and 70% at $\alpha = 45°$ and 90°, respectively). The single-molecule images were captured by an electron-multiplying charge-coupled device (EMCCD) camera (EMCCD1; Cascade II 512, Photometrics) via a $4f$ system of O2 and the L4 lens (AC254-300-A). Alternatively, to have a larger field of view, we used L4 with a shorter focal length ($f = 175$ mm; #47-644, Edmund Optics) and another camera with more pixels (iXon 888, Andor Technology). A lateral (xy) fluorescence image was formed on the EMCCD2 camera (Luca R, Andor Technology) through the L5 lens (AC254-200-A, Thorlabs). We used two quad-band emission filters (FF01-446/510/581/703, Semrock) for AF647 and added a bandpass filter (FF01-590/104, Semrock) for CF568.

System alignment and calibration. We characterized the 3D magnification of our remote-focusing[26] system to correct localization data properly. A group of isolated fluorescent beads was imaged first on EMCCD2 to find a reference focus of O1 ($z = 0$) and the remote focus of O2 at $\alpha = 0°$ was found on EMCCD1 (Supplementary Fig. 9). O1 was then axially stepped by 10 µm over a range of 100 µm, and we sequentially found the corresponding remote focus that yielded in-focus bead images on EMCCD1. From this series of bead images, we extracted the change in lateral magnification over axial depth. We set the L3–O2 distance as a compensator to make the 3D magnification uniform at an emission wavelength of 685 nm (<0.5% distortion; Supplementary Fig. 9).

For two-color obSTORM imaging, the chromatic focal shift present in the detection optics was quantified using a multicolor bead (T7280, Invitrogen) as detailed in Supplementary Fig. 10. After the relative focal shift of the orange channel (570 nm) to the dark-red channel (685 nm) was found, we localized the in-focus PSF images of each channel to identify the pixel registration error. We performed this calibration at α values of 45° and 90° and applied the focal shift during STORM data acquisition and the registration shift during image reconstruction. The calibration using the bead was found to be accurate in dual-color imaging of the same structure in cells (Supplementary Fig. 10).

To achieve 3D obSTORM at $\alpha = 45°$, we placed a cylindrical lens ($f = 200$ mm; LJ1653RM-A, Thorlabs) right in front of EMCCD1 and took a z-stack of dark-red beads (P7220, Invitrogen) by stepping the sample objective (O1) at ~30-nm intervals around $z = 0$. Each bead measurement was repeated four times, and ten beads were measured to extract the size and wobble of PSF. The extracted z-stack data were converted to z_o-stack data by axially scaling with $z_o = z\cos(\alpha)$ and

removing the o-projected shift of PSF by $z\cos(\alpha)$. The calibration data were fitted with fifth- to eighth-order polynomial functions (Supplementary Fig. 19).

Sample preparation. *Fluorescent bead samples.* We used several fluorescent beads (F8800, T7284, P7220 and T7280, Invitrogen) to characterize and calibrate the microscopy system. The (diluted) bead solution was dried on plasma-cleaned #1.5H coverslips and mounted with deionized water on microscope glass slides.

Immunofluorescence of A549 cells. Cells were cultured following standard culture protocols and plated on #1.5H coverslips (CG15CH, Thorlabs) at ~60% confluency. After 24 h, cells were fixed using a solution of 3% paraformaldehyde (PFA) and 0.1% glutaraldehyde in phosphate-buffered saline (PBS) followed by two washes with 0.1% sodium borohydride in PBS. Fixed cells were subsequently blocked and permeabilized in a buffer that contained 3% bovine serum albumin (BSA) with 0.5% Triton X-100 and incubated overnight at 4 °C in primary antibody solutions with anti-α-tubulin (mouse monoclonal, clone DM1α, 1:500; T9026, Sigma) and/or anti-Tom20 (rabbit polyclonal, 1:200; sc-11415, Santa Cruz Biotechnology) antibodies. After triple washes, cells were incubated for 45 min at room temperature in secondary antibody solutions with AF647–anti-mouse (1:500; A31571, Invitrogen) or AF647–anti-rabbit (1:500; A21245, Invitrogen) antibodies and/or CF568–anti-mouse (1:100; 20827, Biotium) or CF568–anti-rabbit (1:100; 20828, Biotium) antibodies.

Immunofluorescence of C. elegans. Young adults at 24 h (post L4) were dissected, and their gonads were immunostained following previously published protocols[27,28]. Fixed tissue was imaged in suspension in polypropylene tubes. The primary antibody was anti-hemagglutinin (HA; mouse monoclonal, clone 2-2.2.14, 1:500; 26183, Invitrogen) for an SYP-4–HA knock-in mutant created from CRISPR–Cas9 as detailed[28], and the secondary antibody used was AF647–anti-mouse (1:500; A31571, Invitrogen).

Immunofluorescence of Drosophila larval brain. Third instar wild-type (w^{1118}) *Drosophila* larvae were filleted to expose the brain and ventral nerve cord in standard HL3 solution (70 mM NaCl, 5 mM KCl, 0.45 mM CaCl$_2$·2H$_2$O, 20 mM MgCl$_2$·6H$_2$O, 10 mM NaHCO$_3$, 5 mM trehalose, 115 mM sucrose and 5 mM HEPES, pH 7.2). The larvae were immediately fixed for 5 min using Bouin's fixative (Ricca Chemical Company), permeabilized in PBS with 0.1% Triton X-100 and blocked in a buffer containing 0.1% Triton X-100, 5% normal goat serum and 0.02% sodium azide. The primary antibodies were anti-Bruchpilot (mouse monoclonal, 1:1,000; nc82, DSHB) and anti-horseradish peroxidase–Cy3 (1:250; 123-165-021, Jackson ImmunoResearch Laboratories). The secondary antibody was AF647–anti-mouse (1:1,000; A21235, Invitrogen).

Immunohistochemistry of mouse retina sections. Freshly enucleated eyes were placed in 4% PFA overnight at 4 °C. Retinas were dissected out, embedded in 5% agarose and cut on a vibratome (60- or 100-µm-thick sections). The sectioned retina was blocked for 2–3 h in 1% BSA and 0.5% Triton X-100 and incubated overnight at 4 °C in anti-PKCα primary antibody (rabbit monoclonal, clone Y124, 1:500; ab32376, Abcam) or anti-Tom20 antibody (rabbit polyclonal, 1:100; sc-11415, Santa Cruz Biotechnology) followed by AF647–anti-rabbit secondary antibody (1:1,000 for PKCα and 1:400 for Tom20; A32733, Invitrogen) for 2 h at room temperature.

Immunohistochemistry of mouse brain sections. A mouse was perfused with 4% PFA, and the brain was fixed in 4% PFA for 2 d and sectioned at 40 µm by a cryostat. The tissue sections were blocked and permeabilized in 3% BSA and 0.5% Triton X-100 for 4 h and incubated in anti-Tom20 primary antibody (rabbit polyclonal, 1:100; sc-11415, Santa Cruz Biotechnology) overnight, followed by AF647–anti-rabbit secondary antibody (1:400; A32733, Invitrogen) for 2 h, all at room temperature.

Immunohistochemistry of stickleback fish. Seven days after fertilization, sticklebacks (*Gasterosteus aculeatus*) were soaked in BrdU (1 mM; B5002, Sigma) for 1 week (solution was replaced daily). At 14 d after fertilization, the specimens were fixed for 4 h at 4 °C in 4% formaldehyde, permeabilized for 30 min in PBS containing 0.5% Triton X-100, underwent antigen retrieval in 2 N HCl for 30 min at room temperature and were blocked for 30 min in PBS containing 2% BSA. The fish were then incubated at room temperature in anti-BrdU primary antibody (mouse monoclonal, 1:500; G3G4, DSHB) followed by AF647–anti-mouse secondary antibody (1:500; A21238, Invitrogen), both in 2% BSA.

Sample mounting. Stained samples were mounted with STORM imaging buffer (Tris-HCl pH 7.5, 100 mM cysteamine, 5% glucose, 0.8 mg ml^{-1} glucose oxidase and 40 µg ml^{-1} catalase) and sealed before imaging. The imaging buffer for *C. elegans* included 1% agarose for sample immobilization. Kapton tapes were used as spacers optionally for thick samples between a glass slide and a #1.5H coverslip.

Image acquisition. We loaded a prepared sample slide on the sample stage and applied water-immersion oil (Immersol W 2010, 444969, Carl Zeiss). We first checked the conventional fluorescence lateral (xy) image on EMCCD2 with

wide-field epi-illumination (~5–20 W cm⁻²), followed by an OPM image on EMCCD1 with light-sheet illumination (~20–80 W cm⁻²). Before STORM imaging, we excited samples at the maximally available laser power for 0–5 min to switch off most fluorophores and lower background fluorescence. Video data were then recorded at 28–50 frames per second (exposure time: 20–35 ms) until 20,000–60,000 frames per color channel were acquired by NIS-Elements AR (Nikon Instruments). We imaged the color channel with a longer emission wavelength (AF647) first and then the CF568 channel at the chromatically adjusted focus to acquire the STORM datasets on the same plane. For volumetric imaging, we took a stack of 45° optical sections (10,000–25,000 frames per section) by stepping the sample objective with an interval of 0.7–1.0 μm (or possibly by y stepping the sample stage). The peak power of light-sheets during STORM imaging was 5–25 kW cm⁻² and 15–70 kW cm⁻² for the 641-nm and 532-nm light, respectively, and 405-nm light (0–10 W cm⁻²) was optionally added to maintain a good single-molecule density.

Single-molecule localization and image reconstruction. Single molecules were detected and located at a pixel accuracy from their bandpass-filtered images as described at http://site.physics.georgetown.edu/matlab. We then cropped each raw PSF image at a fixed window size and fitted them with the two-dimensional elliptical Gaussian model[29], $\frac{a^2 N}{2\pi\sigma_x\sigma_o}\exp\left(-\frac{(x-\mu_x)^2}{2\sigma_x^2}-\frac{(o-\mu_o)^2}{2\sigma_o^2}\right)+b$, where a is the pixel size of images, N is the number of signal photons collected, b is the background fluorescence in photons per pixel and μ_i and σ_i are the center position and the pixelated width of the PSF in the i direction ($i=x,o$), respectively. This initial fitting was performed to update the window size of each molecule (~2×FWHM) and the initial guess for the subsequent least-square fitting solved by MATLAB function 'lsqcurvefit'. The resultant localization precision was calculated analytically[29]. In 3D localization, we used maximum-likelihood estimation[30] for the estimator $\hat{\theta}=[\mu_x,\mu_o,z_o,N,b]$, which absorbs the calibrated polynomial model of the PSF sizes. We discarded single molecules with Cramér–Rao lower-bound[30] precision estimated to be >60 nm in xo or >130 nm in z_o.

The localization data obtained were then compensated as follows. In 3D obSTORM, we corrected the PSF wobble calibrated as a function of z_o, the image distortion in the o direction caused by the cylindrical lens and the o shift between consecutive optical sections by $z\cos(\alpha)$. The non-uniform image magnification was then corrected (Supplementary Fig. 9). For two-color data, we adjusted the relative

pixel registration of the orange (570-nm) channel (Supplementary Fig. 10). The drift of localization data throughout image acquisition was estimated and removed by the correlation approach implemented in PALMsiever[31]. The final data were rendered in PALMsiever or Insight3 (Dr. Bo Huang, University of California, San Francisco). The same localization and compensation procedures were applied to lateral-plane STORM data if acquired together.

Animals. All animal procedures associated with mice and stickleback fish were approved by the Animal Care and Use Committee from the University of California at Berkeley, and complied with all relevant ethical regulations.

Reporting Summary. Further information on research design is available in the Nature Research Reporting Summary linked to this article.

Data availability
The data that support the findings of this study are available from the corresponding authors upon reasonable request.

Code availability
The custom MATLAB codes for the localization analysis used in this study are available as Supplementary Software.

References
25. Bouchard, M. B. et al. *Nat. Photonics* **9**, 113–119 (2015).
26. Botcherby, E. J., Juškaitis, R., Booth, M. J. & Wilson, T. *Opt. Lett.* **32**, 2007–2009 (2007).
27. Phillips, C. M., McDonald, K. L. & Dernburg, A. F. *Methods Mol. Biol.* **558**, 171–195 (2009).
28. Köhler, S., Wojcik, M., Xu, K. & Dernburg, A. F. *Proc. Natl Acad. Sci. USA* **114**, E4734–E4743 (2017).
29. Mortensen, K. I., Churchman, L. S., Spudich, J. A. & Flyvbjerg, H. *Nat. Methods* **7**, 377–381 (2010).
30. Smith, C. S., Joseph, N., Rieger, B. & Lidke, K. A. *Nat. Methods* **7**, 373–375 (2010).
31. Pengo, T., Holden, S. J. & Manley, S. *Bioinformatics* **31**, 797–798 (2015).

natureresearch

Corresponding author(s): Ke Xu, Xiang Zhang

Last updated by author(s): May 1, 2019

Reporting Summary

Nature Research wishes to improve the reproducibility of the work that we publish. This form provides structure for consistency and transparency in reporting. For further information on Nature Research policies, see <u>Authors & Referees</u> and the <u>Editorial Policy Checklist</u>.

Statistics

For all statistical analyses, confirm that the following items are present in the figure legend, table legend, main text, or Methods section.

n/a	Confirmed	
☐	☒	The exact sample size (*n*) for each experimental group/condition, given as a discrete number and unit of measurement
☐	☒	A statement on whether measurements were taken from distinct samples or whether the same sample was measured repeatedly
☒	☐	The statistical test(s) used AND whether they are one- or two-sided *Only common tests should be described solely by name; describe more complex techniques in the Methods section.*
☒	☐	A description of all covariates tested
☒	☐	A description of any assumptions or corrections, such as tests of normality and adjustment for multiple comparisons
☐	☒	A full description of the statistical parameters including central tendency (e.g. means) or other basic estimates (e.g. regression coefficient) AND variation (e.g. standard deviation) or associated estimates of uncertainty (e.g. confidence intervals)
☒	☐	For null hypothesis testing, the test statistic (e.g. *F*, *t*, *r*) with confidence intervals, effect sizes, degrees of freedom and *P* value noted *Give P values as exact values whenever suitable.*
☒	☐	For Bayesian analysis, information on the choice of priors and Markov chain Monte Carlo settings
☒	☐	For hierarchical and complex designs, identification of the appropriate level for tests and full reporting of outcomes
☒	☐	Estimates of effect sizes (e.g. Cohen's *d*, Pearson's *r*), indicating how they were calculated

Our web collection on statistics for biologists contains articles on many of the points above.

Software and code

Policy information about <u>availability of computer code</u>

Data collection	The STORM data was acquired by commercial software, NIS-Elements AR 3.2 (Nikon Instruments).
Data analysis	Single-molecule data was analyzed by custom MATLAB codes (provided as Supplementary Software), open-source MATLAB codes (http://site.physics.georgetown.edu/matlab, http://panda3.phys.unm.edu/~klidke/resources/software/gaussmlev2.zip), open-source PALMsiever (http://code.google.com/p/palm-siever), open-source ImageJ (https://imagej.nih.gov) and Insight3 (Dr. Bo Huang, University of California, San Francisco).

For manuscripts utilizing custom algorithms or software that are central to the research but not yet described in published literature, software must be made available to editors/reviewers. We strongly encourage code deposition in a community repository (e.g. GitHub). See the Nature Research <u>guidelines for submitting code & software</u> for further information.

Data

Policy information about <u>availability of data</u>

All manuscripts must include a <u>data availability statement</u>. This statement should provide the following information, where applicable:
- Accession codes, unique identifiers, or web links for publicly available datasets
- A list of figures that have associated raw data
- A description of any restrictions on data availability

The data that support the findings of this study are available from the corresponding authors upon reasonable request.

Field-specific reporting

Please select the one below that is the best fit for your research. If you are not sure, read the appropriate sections before making your selection.

☒ Life sciences   ☐ Behavioural & social sciences   ☐ Ecological, evolutionary & environmental sciences

For a reference copy of the document with all sections, see nature.com/documents/nr-reporting-summary-flat.pdf

Life sciences study design

All studies must disclose on these points even when the disclosure is negative.

Sample size	No sample size prediction was performed. Statistics were generated from single molecule blinking, which occurs from tens of thousands to millions of times per each single biological sample. As a result, even one sample is sufficient to generate powered statistics for single molecule properties described herein.
Data exclusions	In two-dimensional image reconstruction, we excluded outlying single molecules based on the goodness of fit, the number of signal photons collected, the size of point spread functions and estimated localization precisions. The outliers typically took up 5-15% of the total single molecules acquired in a sample. In three-dimensional (3D) reconstruction, we further excluded the molecules with 3D PSF fit results indicating 1) their z_o locations are out of the considered thickness of an optical section or 2) estimated localization precisions (based on the Cramér-Rao lower bound) are >60 nm in the x (or o) direction or >130 nm in the z_o direction, which were pre-established.
Replication	The reproducibility of super-resolution imaging was measured and verified by comparing single molecule statistics between samples and/or the image quality of standard biological structures (e.g., microtubules or mitochondria) well-established in single molecule localization microscopy. All attempts at replication between individual biological samples were successful.
Randomization	Not relevant. Our study presents a new microscopy method of optical super-resolution imaging.
Blinding	Not relevant. Our study presents a new microscopy method of optical super-resolution imaging.

Reporting for specific materials, systems and methods

We require information from authors about some types of materials, experimental systems and methods used in many studies. Here, indicate whether each material, system or method listed is relevant to your study. If you are not sure if a list item applies to your research, read the appropriate section before selecting a response.

Materials & experimental systems

n/a	Involved in the study
☐	☒ Antibodies
☐	☒ Eukaryotic cell lines
☒	☐ Palaeontology
☐	☒ Animals and other organisms
☒	☐ Human research participants
☒	☐ Clinical data

Methods

n/a	Involved in the study
☒	☐ ChIP-seq
☒	☐ Flow cytometry
☒	☐ MRI-based neuroimaging

Antibodies

Antibodies used	anti-alpha tubulin (Mouse monoclonal, Clone DM1alpha, 1:500, T9026, Sigma), anti-Tom20 (Rabbit polyclonal, 1:200 for A549 cells and 1:100 for mouse retina/brain tissues, sc-11415, Santa Cruz Biotech), AF647-anti-Mouse (1:500, A31571, Invitrogen), AF647-anti-Rabbit (1:500 A21245, Invitrogen), CF568-anti-Mouse (1:100, 20827, Biotium), CF568-anti-Rabbit (1:100, 20828, Biotium), anti-HA (mouse monoclonal, Clone 2-2.2.14, 1:500, 26183, Invitrogen), anti-Brp (Mouse monoclonal, 1:1000, nc82, DSHB), anti-Hrp-Cy3 (Polyclonal, 1:250, 123-165-021, Jackson ImmunoResearch Laboratories), AF647-anti-Mouse (1:1000, A21235, Invitrogen), anti-PKCalpha (Rabbit monoclonal, Clone Y124, 1:500, ab32376, Abcam), AF647-anti-Rabbit (1:1000 for PKCalpha and 1:400 for Tom20 in mouse retina/brain tissues, A32733, Invitrogen), anti-BrdU (Mouse monoclonal, 1:500, G3G4, DSHB), AF647-anti-Mouse (1:500, A21238, Invitrogen).
Validation	All the antibodies used here are commercial products and have been extensively used by us and others in the past, and have been validated through our previous experiments as well as the manufacturer's own test and validations. Additionally, all fluorescence images resulting from the antibodies used matches the expected morphology for each targeted protein with little

to no background labeling. Validation statements for the species and application from the manufacturer's website are listed as follows:
- T9026: Reacts with yeast, human, rat, chicken, fungi, amphibian, bovine, mouse, Suitable for IF, WB
- sc-11415: Reacts with mouse, rat, human, Suitable for ELISA, IF, IHC(P), IP, WB
- A31571: Reacts with mouse, Suitable for FC, ICC, IF, IHC(F), IHC(P), WB
- A21245: Reacts with rabbit, Suitable for ICC, IF, IHC
- 20827: Reacts with mouse, Suitable for FC, IF, WB
- 20828: Reacts with rabbit, Suitable for FC, IF, WB
- 26183: Reacts with Tag, Suitable for ICC, IP, WB
- nc82: Reacts with Drosophila, mosquito, Suitable for IF, IHC, WB
- 123-165-021: Reacts with horseradish peroxidase, Suitable for ELISA, IEP, Hrp detection (Note: this antibody was used only as a reference marker in our study).
- A21235: Reacts with mouse, Suitable for FC, ICC, IF, IHC, IHC(F), IHC(P), IHC(Free)
- ab32376: Reacts with mouse, rat, human, pig, goldfish, Suitable for FC, ICC/IF, IHC(F), IHC(P), IP, WB
- A32733: Reacts with rabbit, Suitable for FC, ICC, IF, IHC, IHC(Free), WB
- G3G4: Reacts with all species labeled with BrdU, Suitable for FACS, FFPE, IF, IHC
- A21238: Reacts with mouse, Suitable for FC/FACS, ICC, IF, IHC

Eukaryotic cell lines

Policy information about cell lines

Cell line source(s)	A549 (ATCC CCL-185)
Authentication	The cell line was not authenticated.
Mycoplasma contamination	The cell line tested was negative.
Commonly misidentified lines (See ICLAC register)	No commonly misidentified cell lines were used in the study.

Animals and other organisms

Policy information about studies involving animals; ARRIVE guidelines recommended for reporting animal research

Laboratory animals	- Caenorhabditis elegans: hermaphrodites, syp-4(ie29[syp-4::HA]), young adults 24 h post-L4 - Drosophila melanogaster: w1118, female, third instar larvae, 6-7 days old - Stickleback fish: Gasterosteus aculeatus, sex was unknown (no known morphological difference between male and female stickleback larvae), 14 days post-fertilization (7 days post-hatch) - Mice: Mus musculus, C57BL/6J, both males and females, 2±1 months old
Wild animals	The study did not involve wild animals.
Field-collected samples	The study did not involve samples collected from the field.
Ethics oversight	All animal procedures associated with mice and stickleback fish were approved by the Animal Care and Use Committee from University of California at Berkeley. No ethical approval was required for Caenorhabditis elegans and Drosophila melanogaster as they are not vertebrates.

Note that full information on the approval of the study protocol must also be provided in the manuscript.